Title : Electron-Scale Dynamics of the Diffusion Region during Symmetric Magnetic Reconnection in Space

R. B. Torbert[1,2], J. L. Burch[2], T. D. Phan[3], M. Hesse[4,2], M. R. Argall[1], J. Shuster[5], R. E. Ergun[6], L.Alm[7], R. Nakamura[8], K. J. Genestreti[8], D. J. Gershman[5], W.R. Paterson[5], D. L. Turner[9], I. Cohen[10], B. L. Giles[5], C. J. Pollock[5], S.Wang[11], L.-J. Chen[11], J. E. Stawarz[12], J. P. Eastwood[12], K.-J.Hwang[2], C. Farrugia[1], I. Dors[1], H. Vaith[1], C.Mouikis[1], A. Ardakani[1], B. H. Mauk[10], S. A. Fuselier[2,13], C. T. Russell[14], R. J. Strangeway[14], T.E. Moore[5], J. F. Drake[11], M. A. Shay[15], Yuri V. Khotyaintsev[7], P.-A. Lindqvist[16], W. Baumjohann[8], F. D. Wilder[6], N. Ahmadi[6], J. C. Dorelli[5], L. A. Avanov[5], M. Oka[3], D. N. Baker[6], J. F. Fennell[9], J. B. Blake[9], A. N. Jaynes[17], O. Le Contel[18], S. M. Petrinec[19], B. Lavraud[20], Y. Saito[21]

Affliations:
[1] University of New Hampshire, Durham, New Hampshire, USA
[2] Southwest Research Institute, San Antonio TX, USA
[3]University of California, Berkeley, USA
[4]University of Bergen, Norway
[5] NASA, Goddard Space Flight Center, Greenbelt, Maryland, USA
[6]University of Colorado Laboratory for Atmospheric and Space Physics, Boulder, Colorado, USA
[7]Swedish Institute of Space Physics, Uppsala, Sweden
[8] Space Research Institute, Austrian Academy of Sciences, Graz, Austria
[9]Aerospace Corporation, El Segundo, California
[10]Johns Hopkins University Applied Physics Laboratory, Laurel, Maryland, USA
[11]University of Maryland, College Park, Maryland, USA
[12]Blackett Laboratory, Imperial College London, London, UK
[13]The University of Texas at San Antonio, San Antonio, Texas, USA
[14]University of California, Los Angeles, Los Angeles, California, USA
[15]University of Delaware, Newark, Delaware, USA
[16]Royal Institute of Technology, Stockholm, Sweden
[17]University of Iowa, Iowa City, Iowa
[18]Laboratoire de Physique des Plasmas, Centre National de la Recherche Scientifique/Ecole Polytechnique/Sorbonne Université/Univ. Paris Sud/Observatoire de Paris, Paris, France.
[19]Lockheed Martin Advanced Technology Center, Palo Alto, California
[20]Institut de Recherche en Astrophysique et Planétologie, Centre National de la Recherche Scientifique, Centre National d'Etudes Spatiales, Université de Toulouse, France
[21]Institute for Space and Astronautical Sciences, Sagamihara, Japan
Japan

One Sentence Summary: NASA's Magnetospheric Multiscale mission detected fast magnetic reconnection and high-speed electron jets in the Earth's magnetotail.

Abstract: Magnetic reconnection is an energy conversion process which occurs in many astrophysical contexts including the Earth's magnetosphere, where the process can be investigated in-situ by spacecraft. We present the encounter of a reconnection site in Earth's magnetotail by the

Magnetospheric Multiscale spacecraft, where reconnection involves symmetric inflow conditions. The electron-scale plasma measurements revealed i) super-Alfvénic electron jets reaching 15,000 km/s, ii) electron meandering motion and acceleration by the electric field, producing multiple crescent-shaped structures in the velocity distributions, iii) the spatial dimensions of the electron diffusion region with an aspect ratio of 0.1-0.2, consistent with fast reconnection . The well-structured multiple layers of electron populations indicate that, despite the presence of turbulence near the reconnection site, the dominant electron dynamics are mostly laminar.

Main Text: Magnetic reconnection is a large-scale plasma process which converts electromagnetic energy to particle energy, and the dominant mechanism by which solar wind energy enters the Earth's magnetosphere. This energy is subsequently dissipated by geomagnetic substorms and aurorae *(1,2)*. Although the consequences of reconnection are large scale, the process starts at the small ion-scale, and even smaller, the electron-scale diffusion region (EDR). Studying the physical processes that cause magnetic reconnection requires determining structures and dynamics inside the EDR with sufficiently high resolution plasma and field measurements (*3*), beyond the capabilities of previous spacecraft missions that have encountered the EDR (*4-6*).

The Magnetospheric Multiscale (MMS) mission focuses on investigating two reconnection regions known to exist around the Earth, the dayside magnetopause and the nightside magnetotail, which host very different plasma parameter regimes. During its first phase (2015-2016), the four MMS spacecraft investigated reconnection in the dayside magnetopause (*3*), where the inflow conditions are highly asymmetric, with different plasma and magnetic pressures in the two inflow regions. In dayside reconnection, magnetic energy conversion processes occur in two separated regions--the X-line, where the magnetic field reverses, and the electron flow stagnation point (*7-8*). In its second

68 phase (2017), MMS explored the kinetic processes of reconnection in the Earth's magnetotail where
69 the inflow conditions are nearly symmetric, the available magnetic energy per particle is more than
70 an order of magnitude higher than on the dayside, and the X-line and stagnation point are coincident
71 (*9*). The amount of magnetic energy per particle in the magnetotail is comparable to that of the solar
72 corona, where magnetic reconnection also occurs.

73 On 11 July 2017, at ~22:34 Universal Time (UT) MMS encountered an EDR when it
74 detected tailward-directed ion and electron jets (negative ion and electron bulk velocities, V_{iL} and
75 V_{eL},, Figures 1f,g) followed by earthward-directed jets, spanning a reversal of essentially the north-
76 south component of the magnetotail magnetic field B_N (Figure 1d) in an intense current sheet (large
77 V_{eM}. We adopt an (LMN) coordinate system to orient the data to the usual 2D view of the magnetic
78 field near a reconnection X-line (Figure 1j), with L in the outflow direction, M along the X-line, and
79 N normal to the current sheet (*10*). The out-of-plane guide field ratio, B_M/B_L, for this event is
80 estimated to be small (< 10% **) (***10***)**. The spacecraft were in the magnetotail at a radial distance from
81 Earth of 22 Earth radii. Four-spacecraft timing of the flow and field reversals indicate that the
82 structure moved away from Earth with velocity V_L~ -170 km/s. These are signatures of a tailward
83 retreat of the reconnection X-line past the spacecraft, as indicated by the MMS path in Figure 1j
84 (*5,6,11-16)*. Except for a brief excursion to the edge of the inflow region, seen in a small
85 perturbation in magnetic field components beginning at 22:34:00UT (due to a flapping of the current
86 sheet), the spacecraft stayed close to the neutral sheet (B_L = 0 plane), indicated by small values of
87 $|B_L|$ (~0-2 nT), during the flow and field reversal. These observations are consistent with crossing
88 both ion and electron diffusion regions, an identification which is supported by the profiles of the ion
89 and electron flows: the out-of-plane electron velocity, V_{eM}, peaked at ~-15,000 km/s, within an order
90 of magnitude of the electron Alfvén speed ($B/\sqrt{(2\mu_0 m_e n_e)}$, where m_e and n_e are electron mass and

density), approximately 20-25,000 km/s. Starting from the X-line (at the $\boldsymbol{V}_{eL}$ and $\boldsymbol{B}$ reversal location) and going left and right in Figure 1h, the electron perpendicular outflow speed $|V_{e\perp L}|$ increased and greatly exceeded the ion speed. While the ion outflow speed ($|V_{iL}|$, Figure 1f) increased with increasing distance from the X-line, $|Ve_{\perp L}|$ reached a peak (~7,000 km/s) before slowing and approaching the ion flow speed at ~22:33:50 before, and ~22:34:20 after, the X-line. Thus, the ends of the ion diffusion region, where the ion and electron outflow velocities are expected to match, are encountered likely near these times. The end of the electron diffusion region, on the other hand, marked by the departure of $Ve_{\perp}$ from $\boldsymbol{E}\text{x}\boldsymbol{B}/B^2$, was confined to a much smaller interval around the X-line, where the electron density reached a symmetric minimum of 0.03 cm^{-3} (electron inertial length, d_e~30 km).

Figures 2a-j (and 3a-e) display MMS3 data in and around the EDR, again in LMN coordinates. Figures 2(k-n) show reduced electron distribution functions (DFs) during the strong reconnecting current (J_M) at times before, and during, the peak of the quantity $\boldsymbol{J}\cdot\boldsymbol{E'}$ (where $\boldsymbol{E'}=\boldsymbol{E}+\boldsymbol{V}_e\times\boldsymbol{B}$), which is the electromagnetic energy conversion rate in the plasma frame, a signature of the EDR (*15*). Although $\boldsymbol{J}\cdot\boldsymbol{E'}$ is mostly positive throughout the period shown in Figure 2, there are some regions with negative values, indicating that the electrons are transferring energy to the electromagnetic field, as seen also in simulations (*17-19*). Figure 3c shows that, at all spacecraft, the signs of E_N and B_L were opposite, consistent with E_N converging toward the neutral sheet (B_L=0) from both hemispheres, as expected for symmetric reconnection with a minimal guide field (*13,15,20,21*). MMS2 (and 4) remained below the neutral sheet (B_L<0 and E_N>0) in the vicinity of the EDR crossing, while MMS1 and 3, located at higher N, made excursions above the sheet, where B_L>0 and E_N<0. This E_N field accelerates the neutral sheet electrons towards the inflow region

where they are accelerated along meandering trajectories (*22*) by the reconnection field, E_M ~1-2 mV/m (Figures 3c,e and **(*10*)**). The electrons were eventually turned towards the L, or exhaust, direction by B_N as they exited the EDR, forming the electron jet seen in figures 2c and 3b on either side of the X-line.

The electron temperature profile in panel 2f shows strong anisotropy from 22:34:01.0 to 02.8 due to magnetic field-aligned electrons in the in-flow region (*4*). During the EDR crossing, there was only a small rise (few 100eV) in parallel or perpendicular temperature (parallel, perpendicular pressure divided by n_e), unlike the case of asymmetric reconnection *(3)*, implying that a substantial fraction of the energy conversion went into the strong electron flows in the M and L directions.

The aspect ratio of the EDR is an approximate measure of the reconnection rate that has not been determined experimentally but has been studied theoretically and with simulations (*4,20,23*). Four-spacecraft timing analysis of the B_N reversal near 22:34:02.2 (see Figure 2a) indicates that the X-line structure was moving tailward (V_{XL}, L component of the X-line velocity, ~ -170 km/s). The EDR length can be estimated by multiplying V_{XL} by the 1/e width of V_{eM} (~3s, Figure 2c), or by the $|V_{eL}|$ peak-to-peak time (~2s, Figure 2d), yielding a full length of 350-500 km (12-17 d_e). MMS also made a brief excursion into the EDR inflow region (beginning at ~22:34:01.0), indicated by the increase in $|B_L|$ and confirmed by the cooler electrons (Figure 2b). By 22:34:02.2, the change in B_L and the timing analysis (V_{XN} ~ -70 km/s) show the structure moving southward, giving MMS also a normal motion into the EDR, reaching the neutral sheet and the peak of the cross-tail current by 22:34:03.0. Using Ampere's Law (*10*), dividing the change in B_L during this normal motion into the EDR (Figure 2a, ~ 22:34:02.0 to 03.0) by the average of J_M, yields a simple estimate of the normal

half-width of 30 km,~1 d_e (*10*). Thus, the aspect ratio is ~0.1 - 0.2, implying a reconnection rate consistent with fast reconnection (*24*).

Multiple crescent and triangular-shaped features in the DF's (Figures 2(k-n) and lower panels of Figure 3) are the result of electron meandering motion in the electromagnetic field structure of the EDR. Figure 2l shows a DF taken at a location below (in N) the EDR, which features multiple crescents, seen as enhanced phase space density at increasing velocities, similar to predictions (*25-27*) and shown in Figure 2q from the simulation of Figure 2o **(***10*). Contrary to magnetopause observations and models (*3,28*), we find more than one crescent. The observations show that crescents at higher $V_{\perp 1}$ are broader in $V_{\perp 2}$ than models predict, i.e., particles with a larger range of $V_{\perp 2}$ bounce twice more than predicted by the model. A likely explanation is that the current sheet electron distribution is more energetic than in the model, but the distributions may be sensitive to even a very small guide field (*29*). Models show that these crescents are generated by the interaction of bouncing electrons with both the normal (E_N) and the reconnection electric field (E_M), and their existence is consistent with canonical momentum conservation. The observation of multiple crescents indicates that the rather complex electron orbits are relatively unperturbed by high frequency fluctuations in the electromagnetic fields. This implies that turbulent effects, which would scatter electrons and hence eliminate distinct phase space features like crescents, do not dominate the particle dynamics in the EDR.

Figures 2(m,n) display a second DF, taken near the X point, which features a pronounced triangular shape in the plane containing *B*, broader at higher energies. Figure 2n shows two enhancements at lower $V_{\perp 1}$ (seen at +/-$V_{\perp 2}$, which is within ~20° of V_N) corresponding to inflowing populations from both above and below the X-line. These enhancements are similar to those

predicted from the simulation shown in figure 2(o-s). In figure 2m, the triangular shape narrows in width as the energy increases, which also appears in the simulation (figure 2r). Bouncing electrons account for this feature: for each bounce, electrons gain successively more energy from acceleration by the reconnection electric field. If electrons have a finite V_L, they eventually interact with the magnetic field in the outflow, and are ejected from the immediate vicinity of the X-line. The acceleration by the reconnection electric field and this ejection explain the triangular shape of the distribution: only electrons with very small V_L remain near the X point long enough to execute multiple bounces and be accelerated to higher energies.

The electron DFs of Figure 3 (lower panels) show the evolution of the above features as MMS entered the EDR. From signatures of the inflow region (*4*), with DFs elongated along *B*, (MMS1 and 2, first column, at 22:34:02.514), the spacecraft, with MMS3 leading, penetrated farther into the current layer and saw accelerated and gyrating electrons growing in energy as time (and N position) increased, showing a perpendicular crescent with energy >1 keV (2×10^4 km/s). By 22:34:02.724, all spacecraft were showing the perpendicular crescents, enhanced flow along the $\boldsymbol{E}\times\boldsymbol{B}$ direction, and also beaming features in the parallel directions. The parallel beams may be responsible for the high frequency electrostatic noise near the upper hybrid frequency (~1200 Hz), seen at this time in Figure 2i (*30*). When the spacecraft were fully within the reconnecting current layer (panel b, 22:34:02.694 -02.757), there were higher energy features rotating into both the $V_{\perp 1}$ (~M) and the $V_{\parallel}$ directions along with persistent counter-streaming, low energy (~10,000 km/s) field-aligned beams. By 22:34:02.757, MMS3, which was deepest in the EDR, saw very energetic electrons in $V_{\perp 1}$, and also in the $-V_{\parallel}$ direction: i.e., these accelerated electrons were rapidly leaving the EDR region. The evolution of many such features can be seen in movie **S1**.

We presented MMS observations of the magnetotail reconnection electron diffusion region, which differs from that on the dayside as it involves symmetric inflow. MMS determined the aspect ratio of the diffusion region (0.1-0.2), which is consistent with simulations of fast reconnection (*7,15,17,24*). The MMS observations of electron dynamics in the diffusion region match predictions made by one class of theories and models – nearly laminar ones that assume the effects of turbulence and associated fluctuations on the electron dynamics are small. Unlike the magnetopause results (*3*), we find that electrons can be accelerated up to three successive times by the reconnection electric field- possibly a consequence of longer confinement in the symmetric magnetic structure. Taken together with MMS observations at the magnetopause, these results provide confirmation that reconnection is an efficient mechanism for the release of magnetic energy, for both geomagnetic substorms and auroral phenomena, and also discriminate between competing theories of reconnection. The energy width of the electron crescents differs from model predictions.

References

1. T. Nagai *et al*., Structure and dynamics of magnetic reconnection for substorm onsets with Geotail observations, *J. Geophys. Res.*103,A3(1998) doi:10.1029/97JA02190.
2. V.Angelopoulos *et al*., Tail Reconnection Triggering Substorm Onset, *Science* 321 (5891), 931-935(2008) DOI: 10.1126/science.1160495.
3. J.L.Burch *et al*., Electron-scale measurements of magnetic reconnection in space, *Science* 10.1126/science.aaf2939 (2016).
4. L.J. Chen*, et al*., Evidence of an extended electron current sheet and its neighboring magnetic island during magnetotail reconnection, *J. Geophys. Res. Sp. Phys*., 113(12), 1–19(2008) doi:10.1029/2008JA013385.
5. T. I. Nagai, *et al*., Construction of magnetic reconnection in the near-Earth magnetotail with Geotail, *J. Geophys. Res.,* 116, A04,222(2011),doi:10.1029/2010JA016283 (2011).
6. M. Oka, *et al*., In situ evidence of electron energization in the electron diffusion region of magnetotail reconnection, *J. Geophys. Res.,* 21(3)(2016), doi: 10.1002/2015JA022040.
7. J.L.Burch,T.D.Phan, Magnetic Reconnection at the Dayside Magnetosphere: Advances with MMS*, Geophys. Res. Lett*., 43(2016), doi:10.1002/2016GL069787(2016).
8. K.J. Genestreti, *et al*., The effect of a guide field on local energy conversion during asymmetric magnetic reconnection: MMS observations, *J. Geophys. Res.: Space Phys.*, *122*, (2017),doi:10.1002/2017JA024247.
9. P.A.Cassak, M.A.Shay Scaling of asymmetric magnetic reconnection: General theory and collisional simulations. *Physics of Plasmas*, *14*(10), 102114(2007),doi:10.1063/1.2795630.
10. Materials and methods are available as supplementary material.
11. M. Øieroset, *et al.*, In situ detection of collisionless reconnection in the Earth's magnetotail, *Nature*, 412, 414–417(2001), doi: 10.1038/35086520.
12. A. Runov, *et al.,* Current sheet structure near magnetic X-line observed by Cluster, *Geophys. Res. Lett.,* 30, 1579(2003), doi: 10.1029/2002GL016730 (2003).
13. A.L. Borg*, et al*., Cluster encounter of a magnetic reconnection diffusion region in the near-Earth magnetotail on September 19, 2003*, Geophys. Res. Lett.,* 32(19), 32–35(2005), doi:10.1029/2005GL023794.
14. V. Angelopoulos., *et al*., Tail reconnection triggering substorm onset., *Science*, 321(5891), 931–935(2008) , doi:10.1126/science.1168045.
15. J.P.Eastwood, *et al.,* Average properties of the magnetic reconnection ion diffusion region in the Earth's magnetotail: The 2001-2005 Cluster observations and comparison with simulations, *J. Geophys. Res.*, 115(A8), A08,215(2010), doi:10.1029/2009JA014962.
16. D.N.Baker, *et al*., Timing of magnetic reconnection initiation during a global magnetospheric substorm onset, *Geophys. Res. Lett*., 29, 2190(2002), doi:10.1029/2002GL015539,
17. S. Zenitani, *et al*., New Measure of the Dissipation Region in Collisionless Magnetic Reconnection, *Phys. Rev. Lett*. **106**, issue 19 (2011).
18. M.A. Shay, Kinetic signatures of the region surrounding the X line in asymmetric (magnetopause) reconnection, Geophys. Res. Lett., 43, 4145–4154(2016), doi:10.1002/ 2016GL069034.
19. P.A. Cassak, *et al*., The effect of a guide field on local energy conversion during asymmetric magnetic reconnection: Particle-in-cell simulations. *Journal of Geophysical Research: Space Physics*, *122*(2017), doi:10.1002/2017JA024555.
20. Shay, M. A. Et al. Structure of the dissipation region during collisionless magnetic reconnection, *J. Geophys. Res.*, **103**, A5, 9165-9176 (1998).

21. J.R.Wygant, *et al.*, Cluster observations of an intense normal component of the electric field at a thin reconnecting current sheet in the tail and its role in the shock-like acceleration of the ion fluid into the separatrix region, J. *Geophys. Res.*, 110, A09206(2005), doi:10.1029/2004JA010708
22. R. Horiuchi, T. Sato, Particle simulation study of driven magnetic reconnection in a collisionless plasma, Physics of Plasmas 1, 3587 (1994), doi:10,1063/1.870894.
23. P. A. Sweet, The Neutral Point Theory of Solar Flares. In B. Lehnert (Ed.), *Electromagnetic Phenomena in Cosmical Physics* (Vol. 6, p. 123) (1958).
24. H.E. Petschek, Magnetic Field Annihilation. *NASA Special Publication*, *50*, 425. Adsabs.harvard.edu/abs/1964NASSP..50..425P(1964).
25. J. Ng, *et al*., Kinetic Structure of the Electron Diffusion Region in Antiparallel Magnetic Reconnection. *Phys. Rev. Lett.*, *106*(6), 65002(2011), doi:10.1103/PhysRevLett.106.065002
26. N. Bessho, N., *et al.,* Electron distribution functions in the electron diffusion region of magnetic reconnection: Physics behind the fine structures. *Geophysical Research Letters*, *41*(24), 8688–8695(2014), doi:10.1002/2014GL062034
27. J. R. Shuster, *et al.*, Spatiotemporal evolution of electron characteristics in the electron diffusion region of magnetic reconnection: Implications for acceleration and heating, *Geophys. Res. Lett*. **42**, 2586-2593(2015).
28. M. Hesse, *et al*., On the electron diffusion region in planar, asymmetric systems. *Geophys. Res. Lett*. **41**, 8673–8680 (2014).
29. J. Ng, et al., Phase space structure of the electron diffusion region in reconnection with weak guide fields, Physics of Plasma, 19, 112108 (2012).
30. W.M. Farrell, *et al.*, The role of upper hybrid waves in magnetic reconnection, *Geophys. Res. Lett., 30*(24)(2003), 2259, doi:10.1029/2003GL017549.
31. M Hesse, *et al.*, The Physical Foundation of the Reconnection Electric Field, *Phys. Plasmas,* 25, 032901 (2018); doi: 10.1063/1.5021461
32. Dunlop, M. W., *et al,* , Analysis of multipoint magnetometer data, *Adv. Sp. Res., 8*(9-10), 273–277, doi:10.1016/0273-1177(88)90141-X (1988).

Acknowledgements

The dedicated efforts of the entire MMS team are greatly appreciated. We are especially grateful to the leadership of the GSFC Project Manager, the late Craig Tooley, his Deputy, Brent Robertson, and the SwRI Payload Project Manager, Ron Black.

Funding

This work was supported by NASA prime Contract No. NNG04EB99C at SwRI, by STFC(UK) grant ST/N000692/1, by CNES, CNRS-INSIS and CNRS-INSU in France, by the Austrian Research Promotion Agency FFG, by NASA Grant NNX14AC78G at the University of Maryland,

by NASA grant NNX08A083G-MMS IDS at the University of California and the University of Delaware, and by the Swedish National Space Board.

Author contributions

Analysis and writing were contributed by (RBT,JLB,TDP,MH,MRA), analysis by (JS,REE,LA,RN,KJG,DLT,SW,LJC,JES,JPE,KJH,CF,ID,CM,AA,CTR,RJS,TEM,JFD,MAS,YVK, MO,ANJ,SMP), electric field data by (RBT,REE,HV,PAL,YVK,FDW,NA), plasma data by (DJG,WRP,BLG,CJP,LJC,SAF,JCD,LAA,BL,YS), magnetic field data by (CTR,RJS,WB,OLC,HV,RBT), and energetic particle data by (DLT,IC,BHM,DNB,JFF,JBB,ANJ).

Data and Materials Availability

All data from MMS are archived at https://lasp.colorado.edu/mms/sdc/public/links/, We used data from the period of 22:29 to 22:37 UT on July 11, 2017, modified as described in (*10).*

Figures

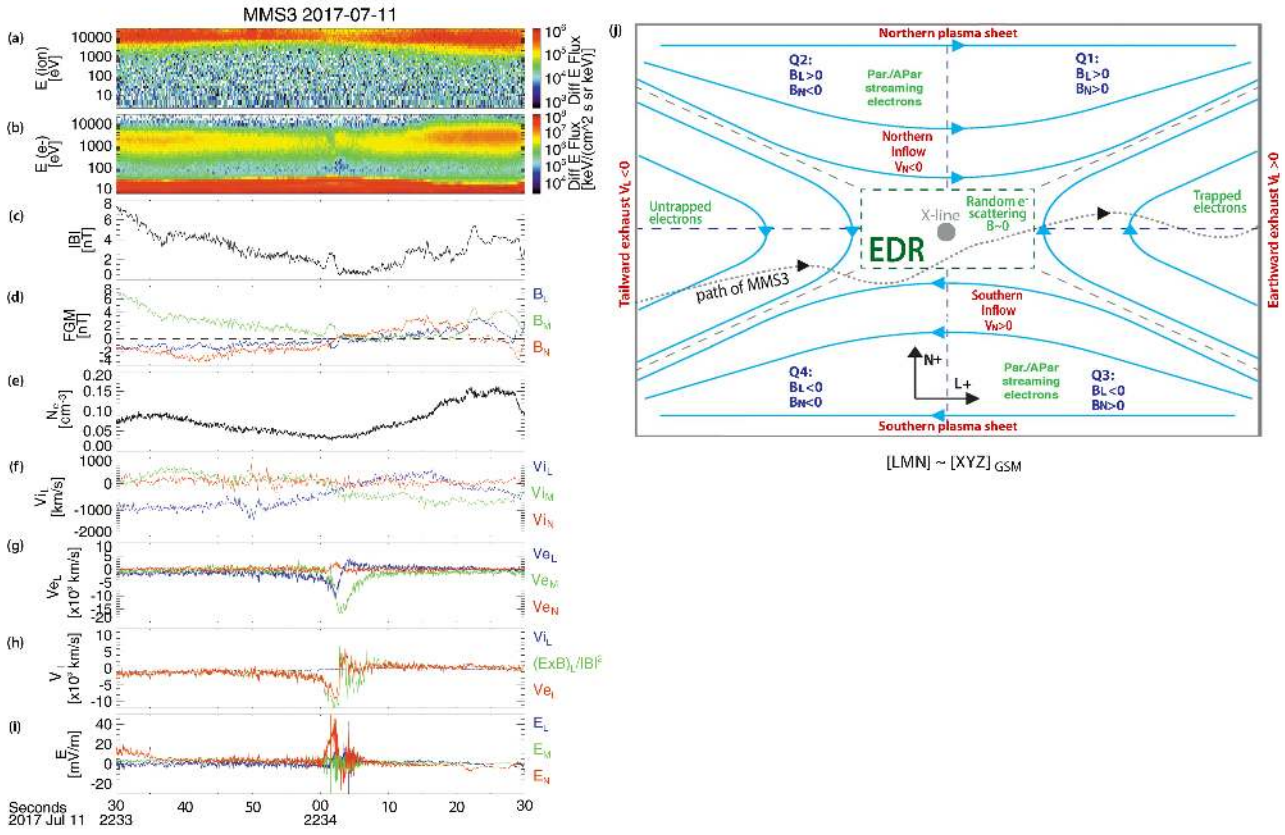

Figure 1. MMS3 summary data near the crossing of the EDR at 223403 on 2017 July 11. (a,b) energy-time spectrograms of ion and electron energy flux, respectively; (c) magnetic field magnitude, and (d) components in the LMN coordinate system, which is very close to the usual Geocentric Solar Magnetospheric (GSM) system (*10*) ; (e) electron density; (f) ion bulk velocity vector; (g) electron bulk velocity vector; (h) the L-component of ion and electron flow perpendicular to $\boldsymbol{B}$, and of $\boldsymbol{E}$x$\boldsymbol{B}/B^2$; (i) **E**, electric field; (j) an illustration of a typical symmetric EDR in the LMN coordinate system, and the expected properties in various quadrants (Q), together with the inferred relative path of the MMS satellites as the X-line retreated tailward.

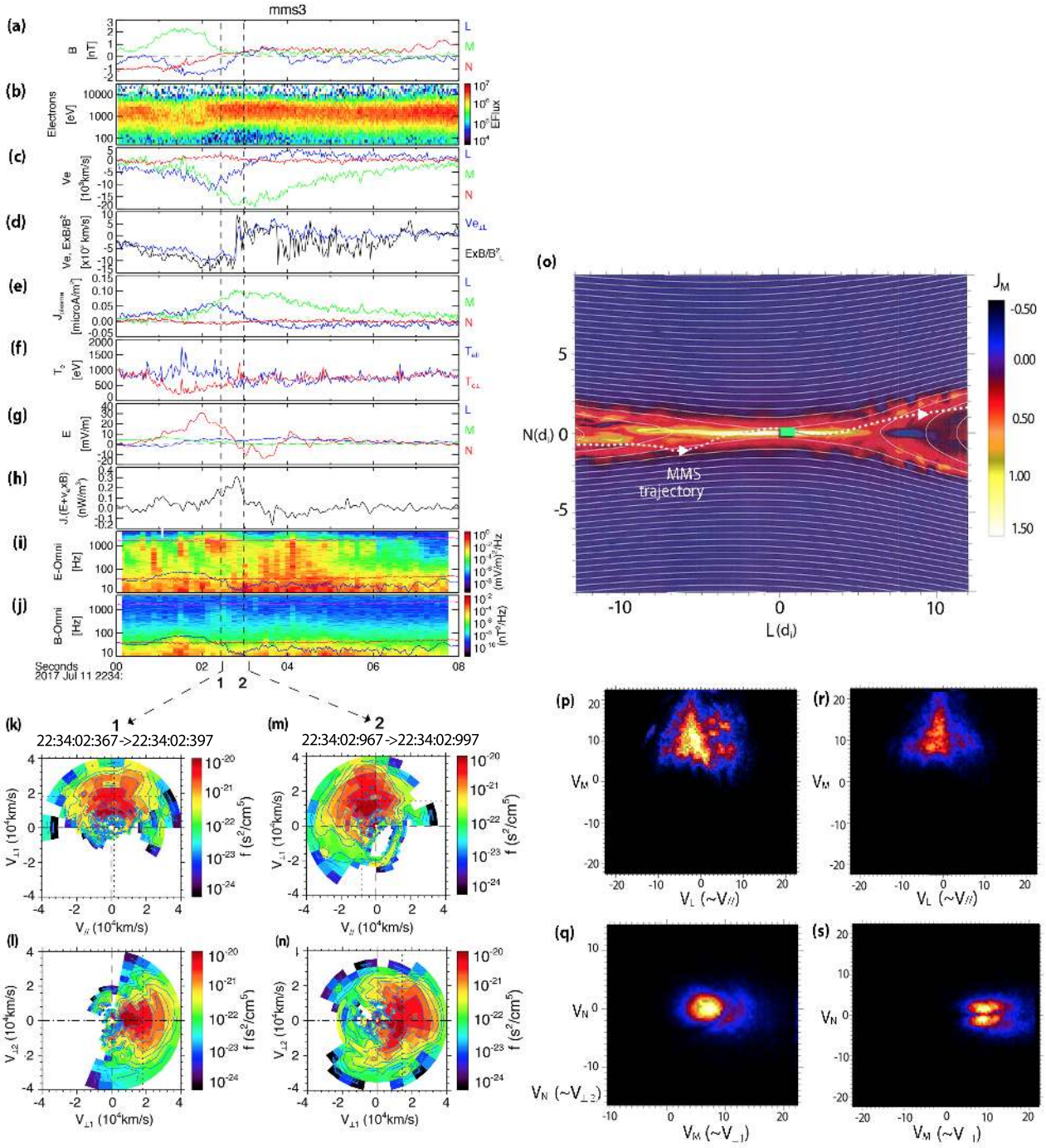

309

310 **Figure 2. MMS3 plasma and field data for 8s from Figure 1 on 2017 July 11.** Panel (a)

311 Magnetic field components in LMN coordinate system; (b) electron omni-directional

spectrogram, with minimum energy set at 50eV to avoid the lower energy spacecraft photoelectrons seen in Figure 1b; (c) electron bulk velocity; (d) L components of $\boldsymbol{V}e_{\perp}$ and $\boldsymbol{E}\times\boldsymbol{B}/B^2$; (e) Current from plasma measurements; (f) $Te_{||}$ and $Te_{\perp}$; (g) Electric field; (h) $\boldsymbol{J}\cdot\boldsymbol{E}'$; (electric (i), magnetic (j)) omni-directional frequency spectrograms, showing the power spectral density of electric or magnetic field fluctuations; (k,l,m,n) electron velocity distribution functions at the times indicated, $V_{\perp 1}$ is $(\mathbf{b}\times\mathbf{v})\times\mathbf{b}$, where **b** and **v** are unit vectors of $\boldsymbol{B}$ and $\boldsymbol{V}_e$; $V_{\perp 2} = \mathbf{v}\times\mathbf{b}$; and $V_{||}$ is the parallel electron velocity. $V_{\perp 1}$ is essentially the $\boldsymbol{E}\times\boldsymbol{B}$ direction and the bulk flow component in that direction is indicated by the dashed vertical lines; (o) Magnetic configuration of a computer simulation *(10),* with color-coded reconnection current (J_M) and the inferred MMS trajectory overlain; (p,q,r,s) Reduced distribution f_e near the green box in (o) from that simulation, with velocity axes (in ion Alfven speed units) corresponding to those of the data in panels k-n. The color code is the same as panel (o), but with simulation units representing phase space density, like those of panels (k-n).

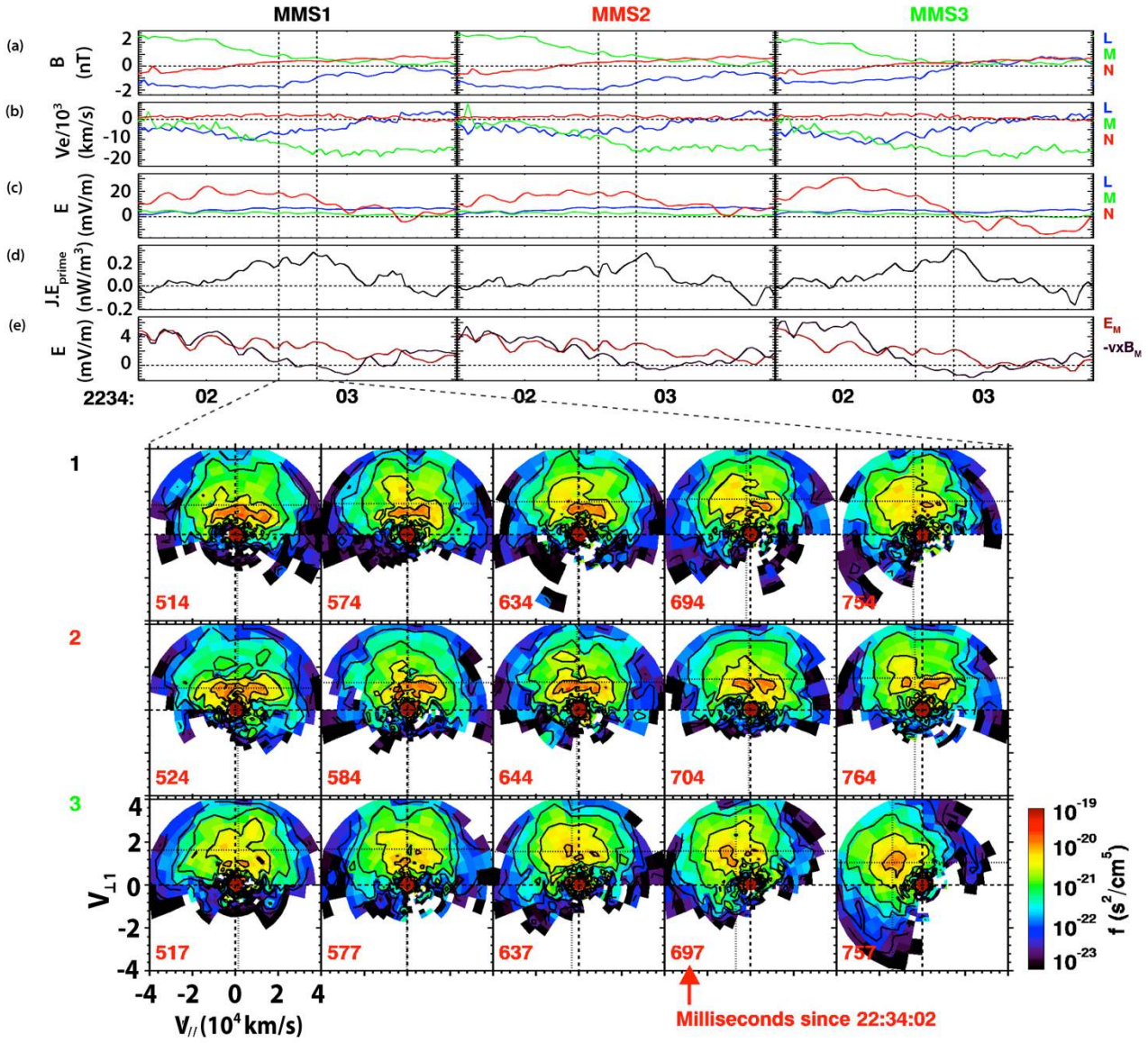

Figure 3. Field data and electron DFs for three MMS spacecraft on 2017 July 11, for ~2 seconds around the EDR. Upper panels, for each spacecraft:(a) components of ***B***; (b) Electron bulk velocity; (c) ***E***, where the reversal in E_N is seen on MMS3 and briefly MMS1, but not MMS2 ; (d) $\boldsymbol{J} \cdot \boldsymbol{E}'$; (e) M-component of ***E*** and -($\boldsymbol{V}_e$ x ***B***); Lower panels, from 2.604s to 2.784s are the reduced (summed over $V_{\perp 2}$) electron 30ms DFs in ($V_{||}$, $V_{\perp 1}$) for each spacecraft at the times between the dotted lines in the upper panels.

Supplementary Materials

Materials and Methods

Figures S1 - S4

Movie S1

Science
AAAS

Supplementary Materials for

Electron-Scale Dynamics of the Diffusion Region during Symmetric Magnetic Reconnection in Space

R. B. Torbert[1,2], J. L. Burch[2], T. D. Phan[3], M. Hesse[4,2], M. R. Argall[1], J. Shuster[5], R. E. Ergun[6], L.Alm[7], R. Nakamura[8], K. J. Genestreti[8], D. J. Gershman[5], W.R. Paterson[5], D. L. Turner[9], I. Cohen[10], B. L. Giles[5], C. J. Pollock[5], S.Wang[11], L.-J. Chen[11], J.E. Stawarz[12], J. P. Eastwood[12], K.- J.Hwang[2], C. Farrugia[1], I. Dors[1], H. Vaith[1], C.Mouikis[1], A. Ardakani[1], B. H. Mauk[10], S. A. Fuselier[2,13], C. T. Russell[14], R. J. Strangeway[14], T.E. Moore[5], J. F. Drake[11], M. A. Shay[15], Yuri V. Khotyaintsev[7], P.-A. Lindqvist[16], W. Baumjohann[8], F. D. Wilder[6], N. Ahmadi[6], J. C. Dorelli[5], L. A. Avanov[5], M. Oka[3], D. N. Baker[6], J. F. Fennell[9], J. B. Blake[9], A. N. Jaynes[17], O. Le Contel[18], S. M. Petrinec[19], B. Lavraud[20], Y. Saito[21]

Affliations:
[1] University of New Hampshire, Durham, New Hampshire, USA
[2] Southwest Research Institute, San Antonio TX, USA
[3]University of California, Berkeley, USA
[4]University of Bergen, Norway
[5] NASA, Goddard Space Flight Center, Greenbelt, Maryland, USA
[6]University of Colorado Laboratory for Atmospheric and Space Physics, Boulder, Colorado, USA
[7]Swedish Institute of Space Physics, Uppsala, Sweden
[8] Space Research Institute, Austrian Academy of Sciences, Graz, Austria
[9]Aerospace Corporation, El Segundo, California
[10]Johns Hopkins University Applied Physics Laboratory, Laurel, Maryland, USA
[11]University of Maryland, College Park, Maryland, USA
[12]Blackett Laboratory, Imperial College London, London, UK
[13]The University of Texas at San Antonio, San Antonio, Texas, USA
[14]University of California, Los Angeles, Los Angeles, California, USA
[15]University of Delaware, Newark, Delaware, USA
[16]Royal Institute of Technology, Stockholm, Sweden
[17]University of Iowa, Iowa City, Iowa
[18]Laboratoire de Physique des Plasmas, Centre National de la Recherche Scientifique/Ecole Polytechnique/Sorbonne Université/Univ. Paris Sud/Observatoire de Paris, Paris, France.
[19]Lockheed Martin Advanced Technology Center, Palo Alto, California
[20]Institut de Recherche en Astrophysique et Planétologie, Centre National de la Recherche Scientifique, Centre National d'Etudes Spatiales, Université de Toulouse, France
[21]Institute for Space and Astronautical Sciences, Sagamihara, Japan
Japan

Correspondence to: roy.torbert@unh.edu

This PDF file includes:

Materials and Methods
Supplementary Text
Figs. S1 to S4
Captions for Movies S1.

Other Supplementary Materials for this manuscript include the following:

Movies S1.

Materials and Methods

Location and Configuration of MMS at 22:34:00 UT on 11 July 2017.

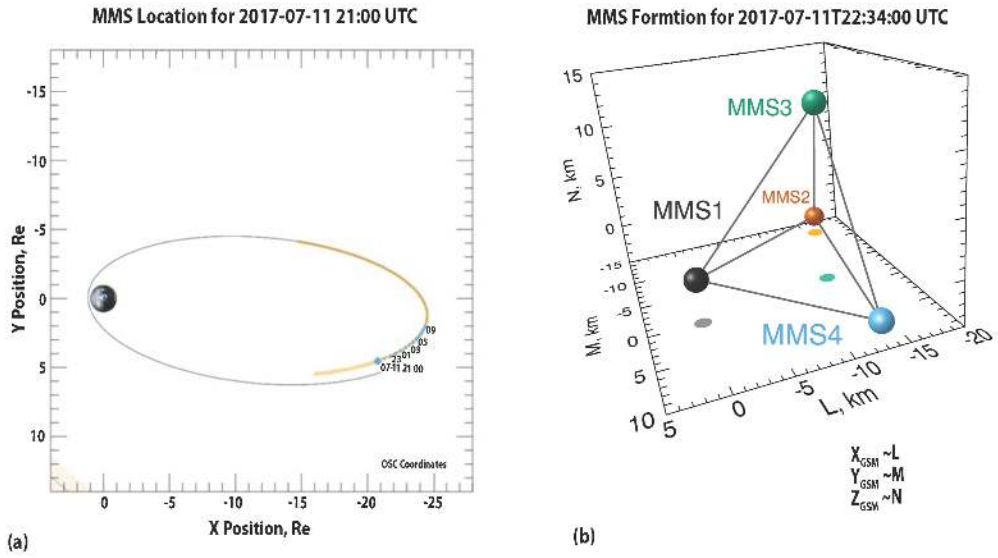

Fig- S1. Location and Configuration of MMS at 22:34:00 UT on 11 July 2017. Panel (a) shows an ecliptic-plane projection of the MMS orbit in geocentric-solar-ecliptic (GSE, nearly inertial) coordinates on 2017 July 11. Times in the orbit are labeled in UT, starting at 21:00. Between 21:00 and 22:00 on this date, mild magnetospheric substorm activity began in the magnetotail. The beige area is the MMS region of interest where high resolution data are taken. **Panel (b)** shows the MMS spacecraft tetrahedral formation in an LMN coordinate system which is very close to the GSM (Geocentric Solar Magnetospheric) coordinates that are typically used to display data in the magnetotail: **X** towards Sun; **Y** perpendicular to Earth's magnetic dipole and **X**, pointing towards dusk; and **Z** = **X** x **Y.**

The LMN coordinate system for the EDR encounter was established by first determining **N** in the direction of the maximum directional derivative in B at 22:34:02s, then determining the **M** vector perpendicular to this **N**, which maximizes the magnitude of the reconnecting current, as seen in Figure 2e, and **L** then is given by **N**×**M**. For this event, [L;M;N] in GSE coordinates are

[0.971, 0.216, -0.106; -0.234, 0.948, -0.215; 0.054, 0.233, 0.971] and, in GSM coordinates, [0.971, 0.219, -0.098; -0.234, 0.956, -0.180; 0.054, 0.197, 0.979]. The LMN unit vectors are all within ~15 degrees of the GSM unit vectors, with X_{GSM} ~ L ; Y_{GSM} ~ M; and Z_{GSM} ~ N, as indicated in the figure. An LMN system can be determined in many different ways, and the several that have been applied for this case are all somewhat similar to the above, but vary by 5-10 degrees. This has a large impact on only one quantity, E_M. Figure 3c shows a normal electric field, E_N, ~30 mV/m, whereas E_M (in figures 2g, 3c, and 3e) is ~1-2 mV/m. Thus, a change in the N-M axes by only 4 degrees can change E_M by 100%. Due to this fact and the underlying uncertainty of the electric field measurement of ~1 mV/m, an estimate of the reconnection rate from the value of E_M is not reliable. Therefore, we have relied on the scalar quantity, $\boldsymbol{J} \cdot \boldsymbol{E'}$ (figures 2h and 3d), which shows that electromagnetic energy is being converted to plasma energy, independent of a particular LMN system.

Guide field (B_M/B_L) estimation

Ideally, the guide field would be determined from the relative angle between the magnetic fields of the two inflow regions. However, this could not be done because MMS did not encounter both lobe regions near the time of X-line crossing. However, it is possible to obtain an estimate of the guide field for this event. The lobe-like magnetic field $|B_L|$ (near 22:31 UT, shown in Figure **S2**) was ~ 13nT, and $|\boldsymbol{B}|$ in the EDR was as low as 0.4nT (Figure 1c, and in Figure 3(a) at ~22:34:02.8 for MMS3), which implies that the guide field B_M was of the order of 0.4nT, but may be somewhat higher due to the effects of the Hall magnetic field. Thus, the normalized guide field $|B_M|/|B_L|$ may be ~4%, but certainly less than 10%.

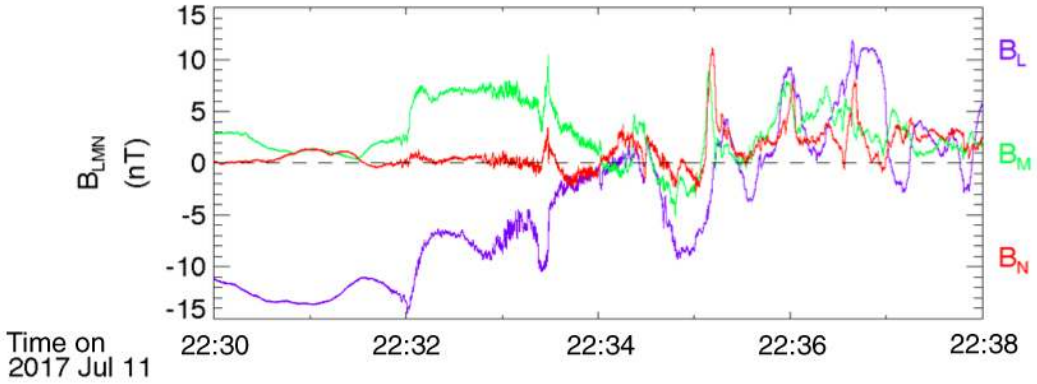

Fig-S2: Magnetic field components in LMN coordinates. Coordinates for this plot were determined using a longer interval (22:31:00 – 22:34:00 UT) than those in the main text. Because of the flapping motion of the current sheet (see in B_L variations) in this interval, the LMN coordinate system is only approximate for data over this long interval.

Computation Details and Calibration Corrections

The ion velocities in figure 1f have been corrected for the fact that the fast plasma sinstrument (FPI) does not cover a sufficient energy range to account for high energy ion phase space when the ion temperature is greater than about 10 keV, as seen in figure 1a. Comparisons over 5 minutes around 22:34:00 with the other ion spectrometer, the Hot Plasma Composition Analyzer, which goes to higher energies, and with the $\boldsymbol{E}\mathrm{x}\boldsymbol{B}/B^2$ velocity show that, during the interval of figure 1, a correction by multiplying the MMS Science Data Center (SDC) data repository values for FPI by a factor of 2, gives values of $\boldsymbol{V}_{\mathrm{ion}}$ that are accurate to within about 20%. In addition, the low density of this EDR encounter resulted in spacecraft potential values greater than 50V. The local photoelectrons from the spacecraft can therefore be seen in figure 1b,

at energies below this value. These electrons were removed in the data of figure 2b by plotting energies only greater than 50eV, and in the computation of the DFs in figures 2 and 3. This same high spacecraft potential affects the offsets of the axial electric field sensor, which then drifts on time scales ~ 10 seconds, the same time scale as the electron density in figure 1e. With running medians over 8 seconds, the offsets of the median electric field were recalibrated to agree with the median of $-\boldsymbol{V}_e \times \boldsymbol{B}$. The electric field was low-pass filtered with a 3 dB point of 8 Hz to correspond to the approximate time dependence of the electron moments.

Using plasma moments, the time profiles of the current peak, from 22:34:01.8 to ~22:34:04.0 in Figure 2e are nearly identical for all four spacecraft, and agree with the curlometer calculation (*32*) of the current from the four spacecraft ($\boldsymbol{J}_{curl}$) at the barycenter of the MMS tetrahedron, except that $\boldsymbol{J}_{curl}$ is a constant fraction (0.8) of the plasma $\boldsymbol{J}$. Because all the profiles are the same in time, the current width must have been greater than the spacecraft separation (~15km). The factor of largest uncertainty is the electron density, which therefore is adjusted to be 0.8 of the SDC value in the calculations below.

A more detailed estimate of the normal half-width of the EDR follows from Ampere's Law:

$$\mu_0 J_M = (\mathrm{curl}(B))_M = (\partial_N B_L - \partial_L B_N).$$

where ∂_N is the partial derivative in the N direction. In our case, B_N is small compared to the other components, and $\partial_L B_N$ even smaller, so we ignore this term. We can thus compute the N position as an integral,

$$N = \int \frac{dB_L}{\mu_0 J_M}$$

over ~1 second from both the rise of the cross-tail current and the appearance of accelerated electrons (~22:34:02.0, Figures 2e,b) to the midplane crossing (i.e. neutral sheet and also current

maximum) at 22:34:03.0. This gives a value of 25 km, a little less that the simple division in the main text. A less reliable estimate follows from timing. As mentioned above, the timing analysis at 22:34:02.2s shows the structure with a normal velocity V_{XN} ~ -70 km/s, but then falls to zero by 22:34:03.0. An average of these two normal velocities (35 km/s), multiplied by the time elapsed above, ~1s , yields an estimate of the EDR normal half-width of ~35 km .We therefore place bounds on this normal width ranging from greater than 15 km (from current profiles) to a higher estimate of 35km, from timing, with the two estimates from Ampere's Law, 25-30km, falling in the middle. We have adopted the simple Ampere value of 30 km for the half-width.

Simulation parameters

The 2D Particle-In-Cell (PIC) simulation shown in figures 2o-r was computed over 3200×3200 grid, a mass ratio m_i/m_e=100, and $7x10^{10}$ particles, of the simulation type described with complete details in (*31*). The initial configuration is a Harris current sheet, with a customary superposed X-type perturbation and a background density of 0.2 in both inflow regions. The ion-electron temperature ratio is 5, and the initial temperature is constant throughout the modeled system. The actual locations of the DFs from this simulation in Figure 2 are: (L=-0.5, N=0.1 for (p,q) and L= 0.5 ,N=0 for (r,s)).

Supplementary Text

Reconnection Topology

The topology of the field lines around the EDR is confirmed by examining pitch angle distributions of the (very) energetic electrons (40-130 keV, Figure **S3**). These data cover 40 seconds around the EDR, which is clearly prominent in the electron velocity peak in Fig. S3 (c). At 22:34:07UT, just Earthward of the EDR, MMS3 detected a burst of energetic electrons in the anti-parallel direction, presumably accelerated in the reconnection process and streaming out along the separatrices. This would be consistent with the return of MMS3 below the neutral sheet on the earthward side of the EDR. Later and further into the exhaust, these electrons are seen filling in the pitch angles (although with enhanced fluxes in the anti-parallel direction) and are now trapped in the Earthward extent of the magnetic field. Tailward of the EDR, before 22:34:00, these electrons are not visible, indicating that they had escaped along field lines connected at both ends to the solar wind. This is evidence of magnetic reconnection on-going at the EDR, and the ability of the reconnection process to accelerate electrons to very high energies, as seen in reconnection in solar flares.

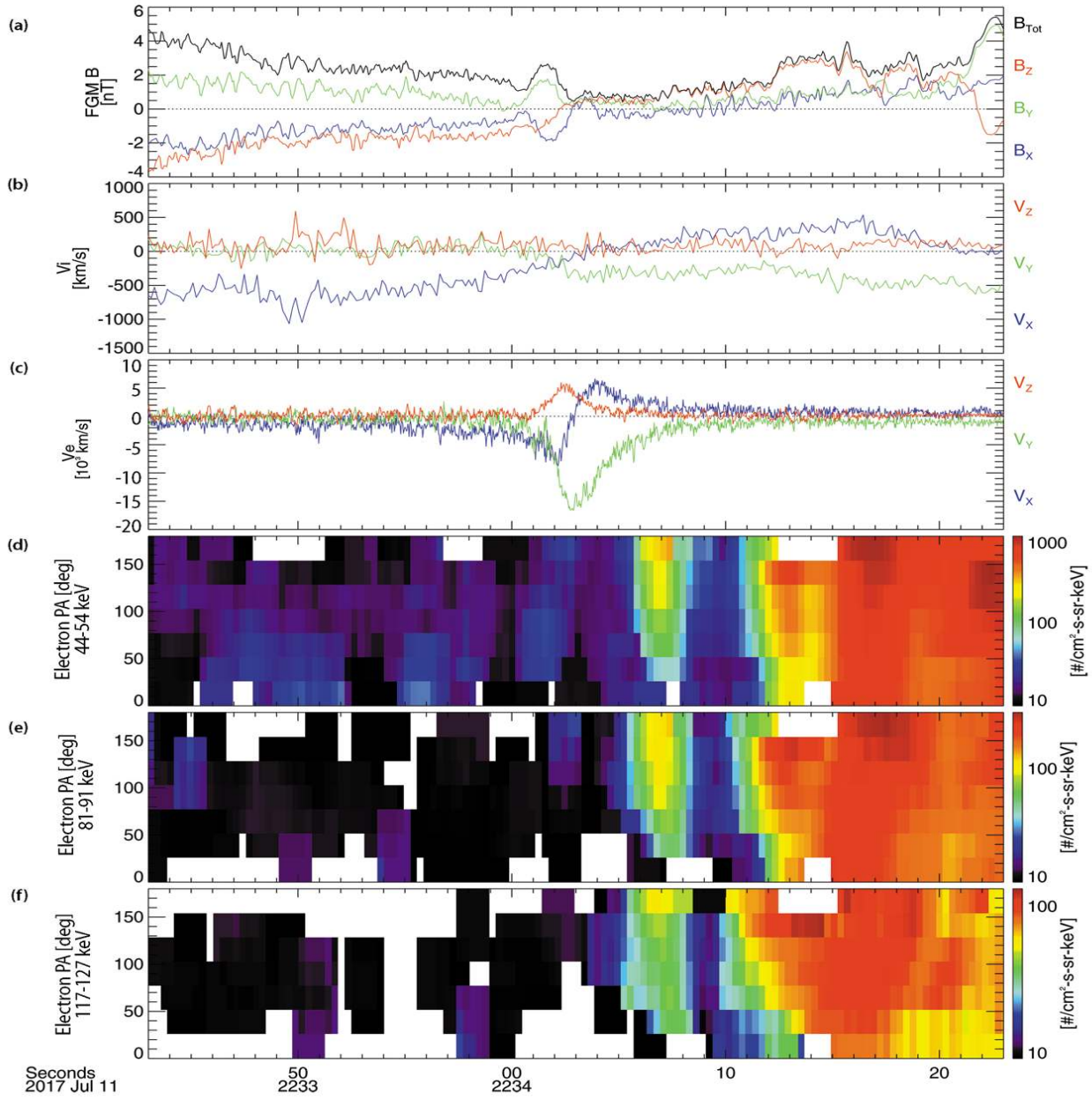

Fig-S3. **MMS3 Energetic Particle and Magnetic Fields.** Magnetic field (a), ion (b) and electron (c) velocities, and electron pitch-angle distributions (d-f) for three selected high energies.

Movie S1.

Electron Velocity-space Distributions. A 6-second segment of burst-mode electron distributions is keyed to a plot of plasma and field data covering the same time period as Figure 2, but from all MMS spacecraft. These distributions are accumulated over four 30ms electron distribution functions to bring out detailed features when the density is as low as $0.03 cm^{-3}$, as in this case. The velocity axes are in the same LMN coordinate system as described above. Figure S4 shows one pane from the animated Movie S1.

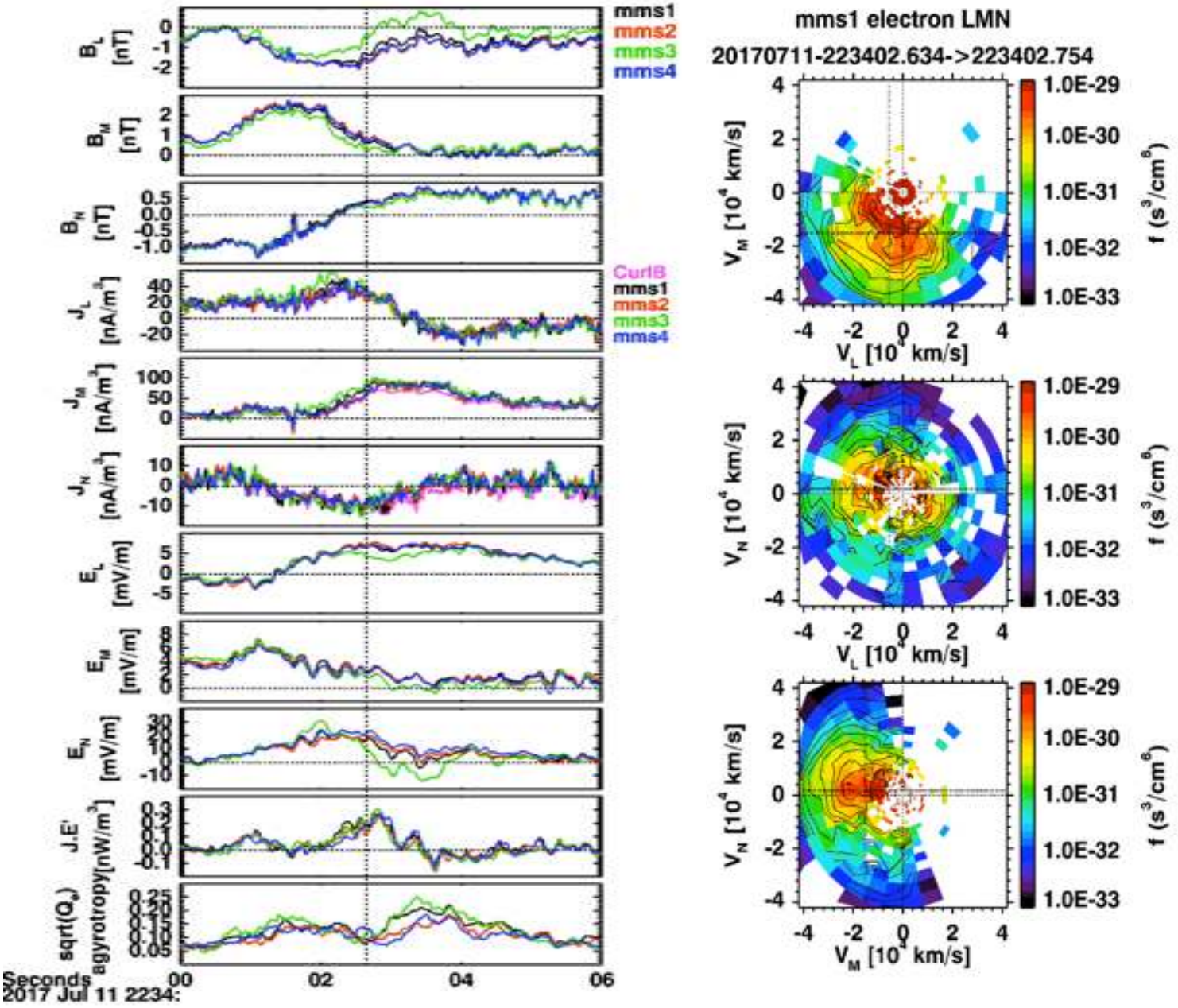

Figure S4, one pane of Movie S1. In the left panel, the time history (from top to bottom) of: B_L, B_M, B_N, J_L, J_M, J_N, E_L, E_M, E_N, $\boldsymbol{J} \cdot \boldsymbol{E'}$, and the Swisdak agyrotropy index, a numerical index indicating agyrotropic features like crescents, for all four spacecraft. The right panel shows the first of four columns (that for MMS1, which is repeated for the other three spacecraft, MMS2-4) that shows the reduced electron distributions for each spacecraft along the indicated LMN velocities at the time of the vertical dash line in the left panel.